

## The Oxidation of Ferritic Stainless Steels in Simulated Solid-Oxide Fuel-Cell Atmospheres

J. E. Hammer,\* S. J. Laney,\* R. W. Jackson,\* K. Coyne,\* F. S. Pettit,\*\*†  
and G. H. Meier\*

Received April 14 2006; revised September 21 2006

---

*The cyclic oxidation of a variety of chromia-forming ferritic stainless steels has been studied in the temperature range 700–900°C in atmospheres relevant to solid-oxide fuel-cell operation. The most detrimental environment at 800°C and 900°C was found to be air with 10% water vapor. This resulted in excessive oxide spallation or rapid scale growth. Impurities in the alloys, particularly Al and Si, were found to have a significant effect on the oxidation behavior. Oxide growth was slow at 700°C but the higher-Cr-content alloys were observed to form sigma-phase at this temperature. The sigma phase formation was accelerated by higher silicon contents, and remarkably, by the presence of water vapor in the exposure environment. Alloys containing Mn were observed to form an outer layer of MnCr<sub>2</sub>O<sub>4</sub> over the chromia scale. The potential for this overlayer to suppress reactive evaporation of the chromia scales has been analyzed.*

---

**KEY WORDS:** oxidation; ferritic steels; interconnects; oxide evaporation; sigma phase.

\*Department of Materials Science and Engineering, University of Pittsburgh, Pittsburgh, PA, USA.

†To whom correspondence should be sent. e-mail: [pettit@engr.pitt.edu](mailto:pettit@engr.pitt.edu)

## INTRODUCTION

Solid-oxide fuel cells provide a potential way to generate electricity with high efficiency and low pollution. The operating principles of fuel cells have been known for over 100 years and low-temperature fuel cells provided the electric power on all the Gemini and Apollo spacecraft. However, fuel cells have not achieved widespread commercial use for a number of economic and technical reasons.

One of the most important technical challenges for planar solid-oxide fuel cells, which operate in the temperature range 700–900°C, is the design of interconnects (current collectors). These components, in addition to drawing off the electric current, must separate the anode compartment of one cell from the cathode compartment of the adjacent cell. This means that one side of an interconnect is exposed to the fuel, typically hydrogen or hydrocarbons in which the oxygen partial pressure is low, and the other side is exposed to the oxidant, which is typically air. The requirements for interconnects have been reviewed recently.<sup>1–4</sup> Interconnect material requirements include a variety of physical, chemical, and electrical properties. The optimal interconnect material would have the following properties:

1. Low electrical resistivity.
2. Impermeability to anode and cathode gases.
3. Stability in both anode and cathode gases under thermal cycling conditions.
4. Chemical compatibility with other cell components.
5. Close match in coefficient of thermal expansion with other components.
6. Good mechanical properties.
7. High thermal conductivity.
8. Ease of fabrication.
9. Low cost.

Metallic interconnects are attractive in that they have favorable values of properties 2, 6, 7, 8, and 9. Metallic materials also have low electrical resistance, but they react with the gases to form oxide layers, which generally have high electrical resistivity. Oxidation resistant alloys are designed to form one of three protective oxides: alumina, silica, or chromia. Of these the electrical resistivities of alumina and silica are much too high for interconnect applications. Exact values of the resistivities of oxides depend on numerous factors but approximate values of the resistivities of silica, alumina, and chromia at 800°C in air are presented in Table I.

**Table I.** Approximate Electrical Resistivities of Oxides in Air at 800°C

Oxide	Resistivity ( $\Omega \cdot \text{cm}^2$ )
SiO <sub>2</sub>	10 <sup>6</sup>
Al <sub>2</sub> O <sub>3</sub>	10 <sup>8</sup>
Cr <sub>2</sub> O <sub>3</sub>	10 <sup>2</sup>

Chromia scales grow much faster than alumina or silica but the resistivity of chromia is sufficiently lower to allow chromia-forming alloys to be considered as a “compromise” as interconnects. The coefficient of thermal expansion of chromia-forming ferritic steels matches that of the ceramic components, particularly in the case of the common anode supported SOFCs. The oxidation behavior of this class of alloy under conditions relevant to SOFC operation is the subject of this paper.

### Previous Studies of Metallic Interconnect Materials

A number of studies have been conducted on chromia-forming metallic-interconnect materials, particularly with regard to their stability in the cathode and anode gases.

#### *Cathode Gas*

The cathode gas provides the oxidant for the cell and will generally consist of air. England and Vircar<sup>5</sup> oxidized thin foils of the commercial Ni-base alloys Inconel 625, Inconel 718, Hastelloy X, and Haynes 230 in air under isothermal conditions at temperatures between 800 and 1100°C. All the alloys formed scales consisting essentially of chromia, and the apparent parabolic rate constants varied over more than an order of magnitude e.g. between  $1 \times 10^{-15}$  and  $2.8 \times 10^{-14}$  g<sup>2</sup>/cm<sup>4</sup>s at 800°C.

Quadackers et al.<sup>6</sup> have studied chromium-base alloys since they have lower coefficients of thermal expansion than the nickel-base alloys. The addition of a Y<sub>2</sub>O<sub>3</sub> dispersion improved the mechanical strength and lowered the oxidation rates of the alloys. A significant problem with Cr (and chromia-forming alloys) which has been recognized for many years<sup>7</sup> is the reactive evaporation of chromia scales. This is a particular problem in the cathode gas since the CrO<sub>3</sub> partial pressure increases with oxygen partial pressure, as illustrated in Fig. 1.<sup>8</sup> The volatile species are reduced at electrochemically active sites on the cathode during SOFC operation, which inhibits the required oxygen reduction.<sup>9</sup> Analysis of the Cr vapor species<sup>10</sup> indicates water contents above about 0.01% in air result in partial pressures of CrO<sub>2</sub>(OH)<sub>2</sub> which exceed the partial pressure of CrO<sub>3</sub>. This will be discussed in more detail in a subsequent section of this paper.

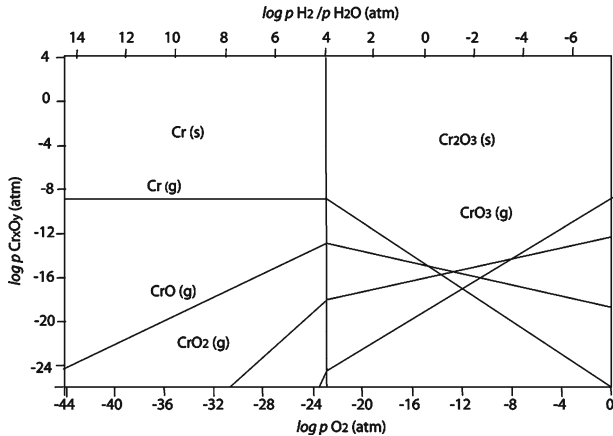


Fig. 1. Vapor species diagram for the Cr-O system at 1250 K from Ref. 7.

A number of investigators have studied the behavior of ferritic stainless steels as interconnect materials since they have a good thermal expansion match with typical ceramic components of SOFCs. Huang et al.<sup>11</sup> studied the isothermal oxidation of ferritic Fe – 26 wt% Cr alloys in air reporting a  $k_P$  of  $8.8 \times 10^{-14} \text{ g}^2/\text{cm}^4\text{s}$  at 800°C. Brylewski et al.<sup>12</sup> reported a similar value of  $8.5 \times 10^{-14} \text{ g}^2/\text{cm}^4\text{s}$  for Fe-16 wt% Cr. Quadakkers et al.<sup>13,14</sup> have developed model alloys based on the philosophy of:

- i. Using La additions to slow the growth rate of the chromia scale and improve the adherence of the scale to the alloy.
- ii. Making additions of Ti and Mn to form spinels on the chromia scale to reduce  $\text{CrO}_3$  evaporation.
- iii. Maintaining Al and Si levels as low as possible to prevent the formation of electrically insulating alumina or silica layers.

(The last point is quite important in that many commercial Fe- and Ni-base alloys, which are nominally chromia-formers, contain sufficient Al and/or Si so that, under certain exposure conditions, alumina or silica can form between the chromia layer and the alloy.)

The work of Quadakkers et al has lead to the commercialization by ThyssenKrupp VDM of a ferritic alloy, Crofer 22 APU, specifically designed for fuel-cell applications. Yang et al.<sup>15</sup> have reported the results of cursory studies of the oxidation behavior of this alloy.

The area specific resistance (ASR) was reported in Ref. 11 for scales formed during 24 h exposures in air at 900°C. The ASR measured at 900°C with Ag electrodes was on the order of 0.02  $\Omega\text{cm}^2$ . Quadackers et al.<sup>13</sup> performed in-situ measurements of the ASR of chromia scales forming at 800°C on one of the modified ferritic alloy alloys described above. The ASR (measured at 800°C) after 100 h of oxidation was approximately 0.01  $\Omega\text{cm}^2$  and increased to approximately 0.1  $\Omega\text{cm}^2$  after 8000 h.

#### *Anode Gas*

The anode gas consists of the fuel (typically hydrogen or hydrocarbons) and the products of combustion (water vapor and, possibly, CO and CO<sub>2</sub>). England and Vircar<sup>16</sup> oxidized thin foils of the commercial Ni-base alloys Inconel 625, Inconel 718, Hastelloy X, and Haynes 230 in hydrogen, which was saturated with water at 40°C under isothermal conditions at temperatures between 700 and 1100°C. The growth rate of the chromia scales at 800°C were higher than those observed in air<sup>5</sup> for the same alloys and the electrical resistance of the scales was higher than for those formed in air.

Quadackers et al.<sup>17-19</sup> have studied pure Cr and yttria-dispersed Cr at 950 and 1000°C in Ar/H<sub>2</sub>/H<sub>2</sub>O mixtures. They too observed larger mass gains in H<sub>2</sub>/H<sub>2</sub>O mixtures but correctly point out that this is the result of mass losses from CrO<sub>3</sub> evaporation in air, which are minimal at the reduced oxygen partial pressures in H<sub>2</sub>/H<sub>2</sub>O mixtures. One rather surprising result of this study was that the chromia scales were substantially more adherent when formed in H<sub>2</sub>/H<sub>2</sub>O mixtures than in dry air. It is well documented that spallation of alumina scales is accelerated by water vapor<sup>20,21</sup> so these results for chromia are in need of further study.

Quadackers et al. reported the chromia scales formed on ferritic stainless steels in simulated anode gas at 800°C were thinner than those formed in air<sup>13,14</sup>. Brylewski et al.<sup>12</sup> reported similar values of  $k_p$  for oxidation in 94H<sub>2</sub>/6H<sub>2</sub>O and air.

#### *Dual-Atmosphere Exposures*

Yang et al.<sup>22</sup> observed a change in the oxide formed on stainless steels in air when a simulated anode gas was present on the opposite side of the specimen. They hypothesized that this is the result of H diffusing from the anode side and affecting the oxide growth on the cathode side.

This paper presents results for the oxidation of ferritic stainless steels in single atmospheres which form a baseline for understanding oxidation in dual atmosphere conditions.

## EXPERIMENTAL PROCEDURES

### Cyclic Oxidation

The cyclic oxidation of a range of ferritic stainless steels has been evaluated under a range of conditions pertinent to fuel-cell operation. The alloys were: (Nominal compositions in Wt%)

- E-BRITE (Fe-26 Cr-1 Mo – 0.2 Si)
- 26Cr Ferritic (Fe-26Cr-1-Mo-2Mn-4.5Ni-1Si-1Al)
- AL 453 (Fe-22 Cr-0.6 Al-0.3 Mn + 0.1Ce/La)
- Crofer22 APU (Fe-22Cr-0.5Mn-0.08 Ti-0.016P-0.06 La)

The exposure conditions included:

- $T = 900^{\circ}\text{C}$  and  $700^{\circ}\text{C}$  (Limited experiments were performed at  $800^{\circ}\text{C}$ )
- One-Hour Cycles (45 min. hot, 15 min. cold)
- Atmospheres
  - Dry Air (Simulated Cathode Gas)
  - Air + 0.1 atm  $\text{H}_2\text{O}$  (Simulated Moist Cathode Gas)
  - Ar/ $\text{H}_2$ / $\text{H}_2\text{O}$  (Simulated Anode Gas) ( $p_{\text{O}_2} = 10^{-17}$  atm at  $900^{\circ}\text{C}$  and  $10^{-20}$  at  $700^{\circ}\text{C}$ )

The exposure apparatus used for these exposures is shown schematically in Fig. 2.

### Specimen Characterization

Following exposure the oxidation products and alloy microstructure were characterized using X-ray diffraction (XRD), scanning-electron microscopy (SEM) and energy-dispersive X-ray analysis (EDS).

## RESULTS AND DISCUSSION

### Cyclic Oxidation at $900^{\circ}\text{C}$

The experiments at  $900^{\circ}\text{C}$  were designed as *accelerated tests*. The duration of the test was 2000 cycles, which corresponded to 1500 h at temperature ( $900^{\circ}\text{C}$ ). Based on the temperature dependence of the parabolic rate constants reported for oxidation of Fe-26 wt% Cr in air,<sup>11</sup> exposure for 1500 h at  $900^{\circ}\text{C}$  should result in a chromia-scale thickness comparable to that formed after about 16,000 h at  $800^{\circ}\text{C}$ . Thus, if one can assume the same

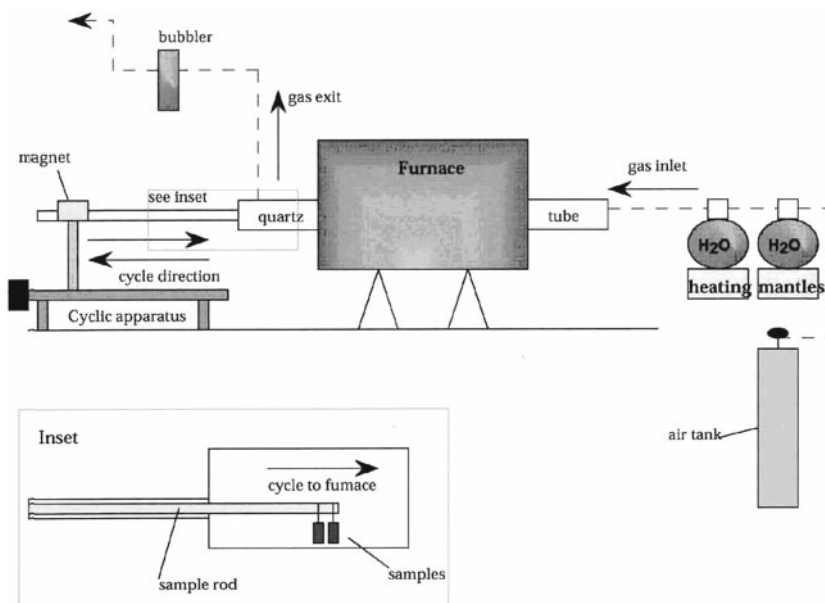


Fig. 2. Schematic diagram of the apparatus used for cyclic oxidation exposures with controlled partial pressures of water vapor.

oxidation mechanisms at 800 and 900°C, these experiments should simulate an exposure at 800°C for 16,000 h of hot time. In the latter case 2000 cycles would correspond to the specimen being cycled to room temperature with a frequency of approximately twice per day. Since cyclic degradation can depend on cycle frequency, it is not clear how many cycles at 800°C would produce similar degradation. Correlation between the accelerated tests with operating conditions is an ongoing theme of this project.

The oxidation kinetics for exposure in dry air (simulated cathode gas) are presented in Fig. 3. The mass gains for Crofer22 APU correspond to literature values for the isothermal oxidation of ferritic alloys in air<sup>11</sup> while the mass gains for Fe-26Cr ferritic are somewhat smaller and those for Al 453 are somewhat larger. The oxidation curves do not give evidence for substantial scale spallation. The results for duplicate specimens under all exposure conditions were in good agreement. Therefore, subsequent plots will present the average data for the two specimens in a single curve.

Figure 4 presents the corresponding oxidation kinetics in simulated anode gas. The mass gains for Fe-26 Cr ferritic and Crofer are similar and are similar to those reported for isothermal oxidation of ferritic alloys in hydrogen-water vapor atmospheres.<sup>12</sup> The mass gains for AL 453 are larger.

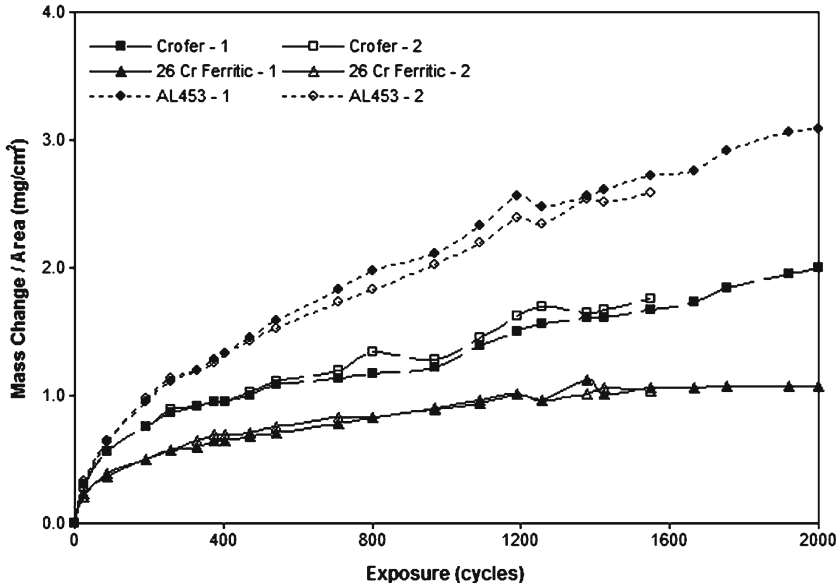


Fig. 3. Weight Change vs Time plots for duplicate specimens of ferritic alloys exposed in dry air (simulated cathode gas) at 900°C using 1-hour cycles.

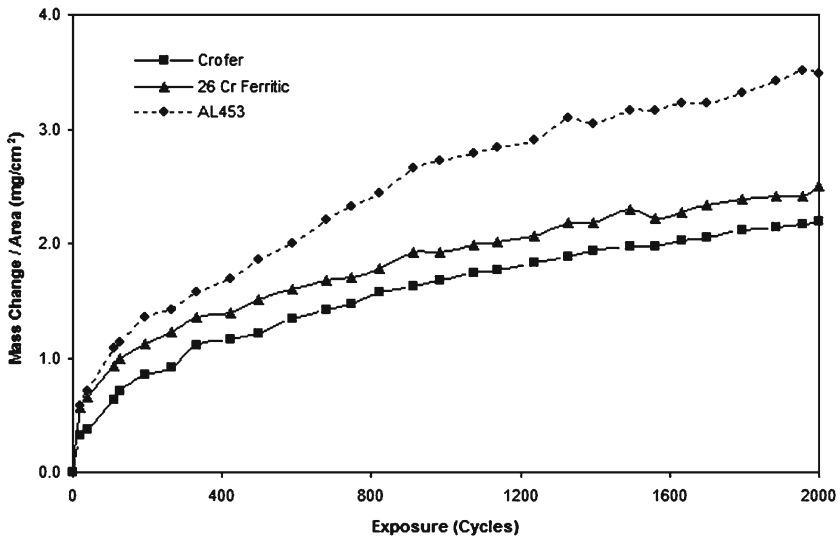


Fig. 4. Weight Change vs Time plots for duplicate specimens of ferritic alloys exposed in Ar/H<sub>2</sub>/H<sub>2</sub>O (simulated anode gas) at 900°C using 1-hour cycles.



Figure 5 presents the oxidation kinetics in air containing 10% water vapor. This gas does not directly simulate a fuel-cell atmosphere. However, with the use of air, there are the possibilities that the air has not been dried, small seal leakages occur, or hydrogen diffuses to the cathode side and reacts with oxygen; therefore, it is not unreasonable to anticipate that the cathode gas may contain water vapor in some situations. The mass changes for Fe-26Cr ferritic are similar to those in dry air. However, the mass gains are far larger for Crofer, and AL 453 than those observed in either of the other two atmospheres. These observations are consistent with measurements of oxide thickness (presented in Table II) and metallographic observations to be described below. It is important to note that the simple analysis in the table can be compromised by both specimen deformation and internal oxidation, particularly in the case of Crofer, yielding significant differences between measured and calculated values.

Figure 6 presents cross-section micrographs of Fe-26Cr ferritic after exposures in all three atmospheres at 900°C. The scales are similar and are consistent with the similar oxidation kinetics observed in the three environments. The external scale consists of  $\text{Cr}_2\text{O}_3$  and there is a fine distribution of Al-rich precipitates in the alloy below the scale. Figure 7 shows more detail of the alloy/scale interface for Fe-26Cr. There is a substantial amount of silica at this interface. It is not clear if this phase was responsible for the

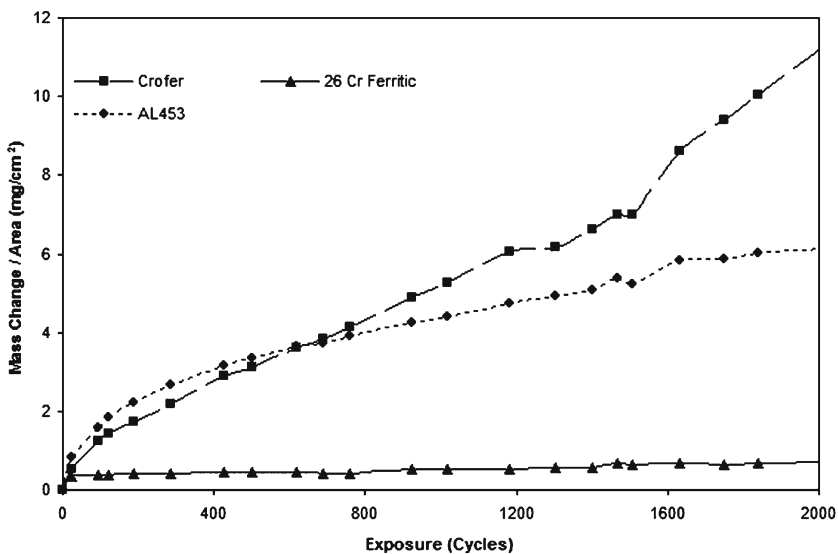


Fig. 5. Weight Change vs Time plots for duplicate specimens of ferritic alloys exposed in air + 10%  $\text{H}_2\text{O}$  (simulated moistened cathode gas) at 900°C using 1-hour cycles.

**Table II.** Comparison of Oxide Thicknesses and Weight Gains per Area for Three Ferritic Alloys Exposed at 900°C in Ar/H<sub>2</sub>/H<sub>2</sub>O, air, and air + 10% H<sub>2</sub>O

Alloy	Atmosphere	Time (h)	Average Oxide Thickness (μm)	Calculated Δm/A (mg/cm <sup>2</sup> )	Measured Δm/A (mg/cm <sup>2</sup> )
Crofer	Dry Air	2000	8	1.3201	2.1916
Crofer	Air + 0.1 atm H <sub>2</sub> O	2000	13.5	2.2276	1.9964
Crofer	Ar/H <sub>2</sub> /H <sub>2</sub> O	2005	20	3.3001	11.2230
AL 453	Dry Air	2000	8.75	1.4444	2.5033
AL 453	Air + 0.1 atm H <sub>2</sub> O	2000	7.5	1.2375	1.0790
AL 453	Ar/H <sub>2</sub> /H <sub>2</sub> O	2005	11.5	1.8976	0.7079
Fe-26Cr	Dry Air	2000	4.5	0.7425	3.4825
Fe-26Cr	Air + 0.1 atm H <sub>2</sub> O	2000	6	0.9900	3.0840
Fe-26Cr	Ar/H <sub>2</sub> /H <sub>2</sub> O	2005	8.5	1.4025	6.1166

lack of acceleration of scale growth for exposures in air + 10% H<sub>2</sub>O. However, it is believed that oxide spallation is primarily responsible for the thinner scales observed on Fe 26 Cr in this atmosphere. Figure 8 shows a macroscopic surface photograph of Fe-26Cr ferritic after 847 cycles showing circular spalled areas. Other areas were also observed where there were circular areas of thin oxide, which appeared to have reformed in spalled areas on subsequent cycles. Spalling is also consistent with the data in Table II. The experimental mass gain for Fe-26Cr Ferritic in wet air is substantially smaller than that calculated from the oxide thickness. The mass changes in air + 0.1 atm H<sub>2</sub>O may also be influenced by evaporation of CrO<sub>2</sub>(OH)<sub>2</sub>, as will be discussed below.

Figure 9 presents cross-section micrographs of Crofer after exposure in all three environments. The specimen exposed in dry air had a continuous layer of MnCr<sub>2</sub>O<sub>4</sub> at the scale/gas interface with a chromia layer beneath. Figure 10 indicates some internal oxidation below the chromia layer. These oxides were found to be Al-rich, although Al is not listed as an intentional component of this alloy. The specimen exposed in wet air exhibited a very thick scale, which is consistent with the large mass gain in this atmosphere. However, the MnCr<sub>2</sub>O<sub>4</sub> is present as discontinuous particles at the scale/gas interface rather than as a continuous layer. Figure 11 shows a macroscopic photograph of a Crofer specimen oxidized in wet air. This specimen is severely warped, presumably because of the extensive oxidation. Specimens exposed in dry air and simulated anode gas did not exhibit this deformation. The specimen exposed in simulated anode gas showed very little MnCr<sub>2</sub>O<sub>4</sub> at the scale/gas interface and the chromia scale appeared somewhat "friable". The micrograph of this specimen in Fig. 10 also shows an inclusion running parallel to the rolling direction of the sheet. This was identified

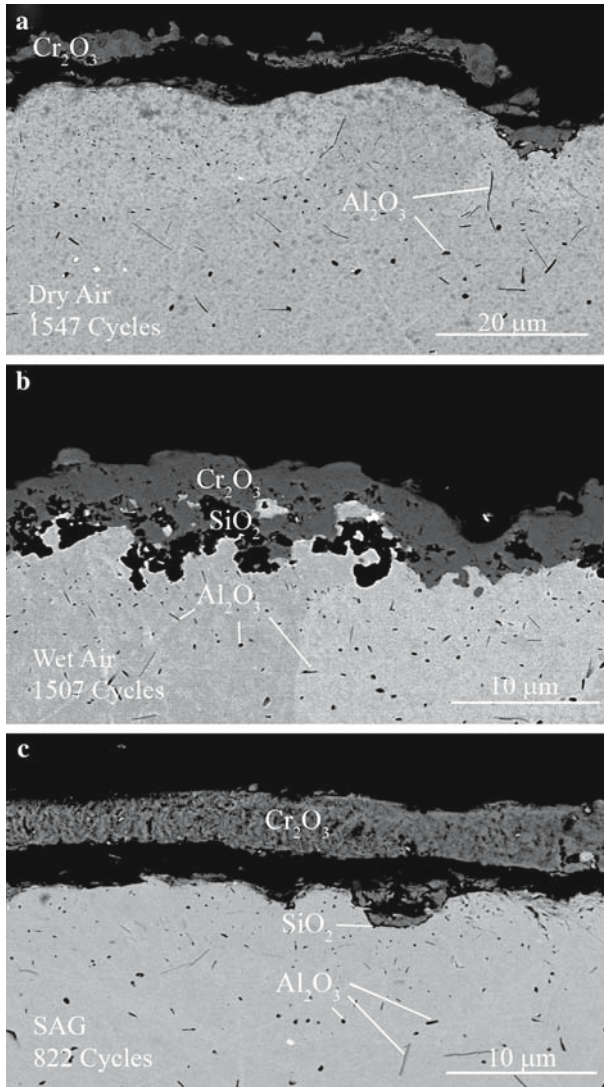


**Fig. 6.** Cross-section micrographs of Fe-26%Cr ferritic after exposure in dry air (a), air + 10%  $\text{H}_2\text{O}$  (b), and  $\text{Ar}/\text{H}_2/\text{H}_2\text{O}$  (c) atmospheres at 900°C.

as a La-rich oxide. Similar inclusions, as well as Ti-nitrides were found throughout the as-received alloy.

Figures 12 and 13 present cross-section micrographs of AL 453 exposed in the three environments. The striking feature in all environments

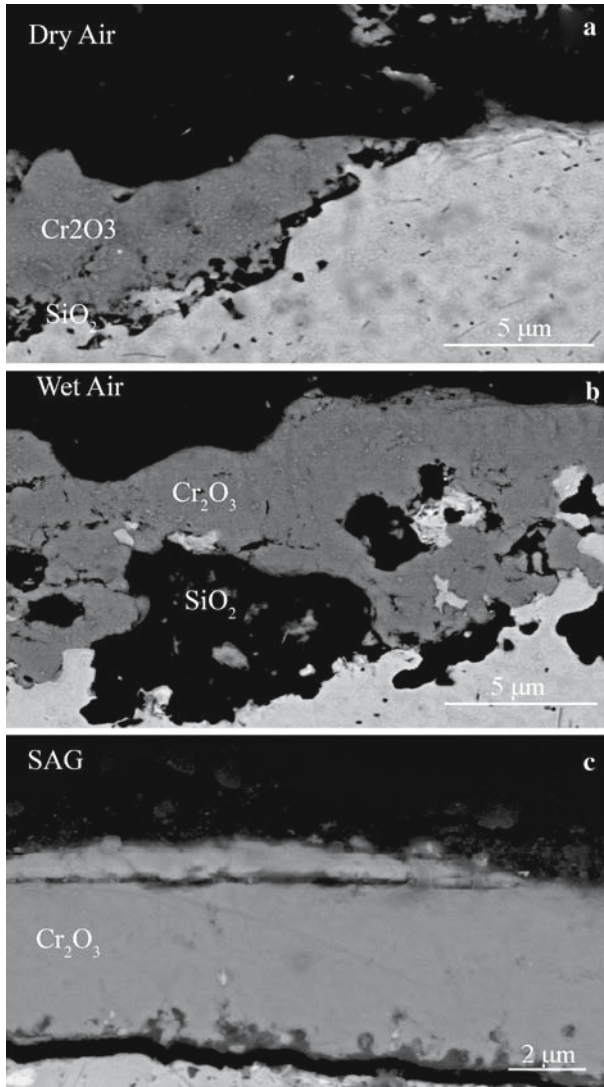


**Fig. 7.** Cross-section micrographs of Fe-26%Cr ferritic after exposure in dry air (a), air + 10% H<sub>2</sub>O (b), and Ar/H<sub>2</sub>/H<sub>2</sub>O (c) atmospheres at 900°C showing details of the alloy/scale interface.

is the extensive internal oxidation of Al below the chromia scale. Table II indicates the measured mass gain of this alloy in all three environments is substantially larger than that calculated from the thickness of the external

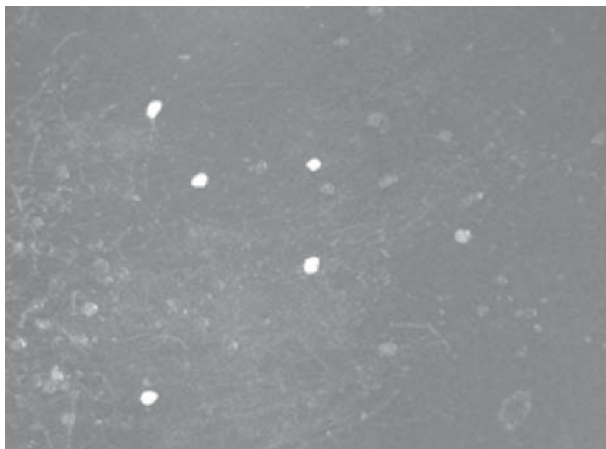


**Fig. 8.** Macroscopic photograph showing freshly spalled and re-grown areas on the surface of Fe-26Cr Ferritic (847 cycles, 1/10 atm H<sub>2</sub>O).

scale. The oxygen uptake in forming the internal oxides is responsible for this difference. An additional feature of this alloy is the appearance of a layer of metallic Fe–Cr between the internal-oxidation zone and the external chromia scale. The origin of this layer has not yet been determined. One possibility is extrusion of metal out from the zone of internal oxidation as the alumina precipitates form. This phenomenon is discussed more fully below.

In summary, accelerated cyclic-oxidation testing at 900°C has been investigated. The most detrimental environment was found to be air with 10% water vapor. This resulted in excessive oxide spallation from Fe-26Cr ferritic and rapid scale growth on Crofer22 APU and AL 453. Huczowski et al.<sup>23</sup> have explained the accelerated oxidation of Crofer as resulting from the internal oxidation of Si and Al causing metallic protrusions. This presumably increases the effective surface area of the alloy. However, Fig. 9 does not indicate a significant difference in the amount of internal oxidation or metal protrusions between the specimens exposed in dry air and air plus water vapor. Therefore, it is not clear why the scale on Crofer grows faster in the presence of water vapor.

### **Cyclic Oxidation at 800°C**

The accelerated oxide growth rate on Crofer at 900°C, when exposed in air with 10% water vapor, prompted further investigation of this phenomenon at 800°C. In addition to Crofer several other alloys were studied.

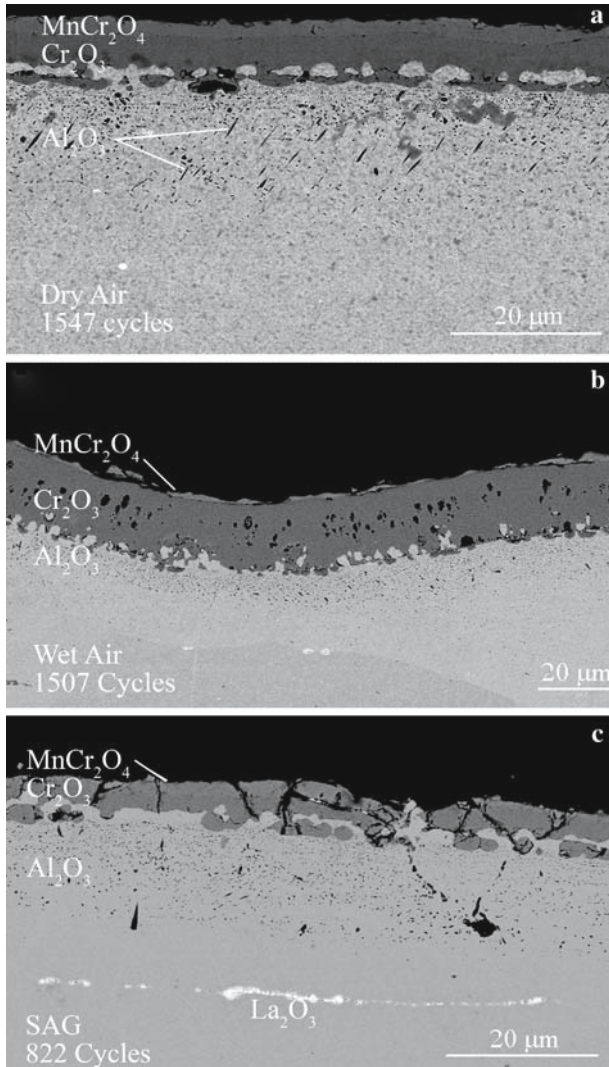


**Fig. 9.** Cross-section micrographs of Crofer after exposure in dry air (a), air +10% H<sub>2</sub>O (b), and Ar/H<sub>2</sub>/H<sub>2</sub>O (c) atmospheres at 900°C.

These included JS-3, a model alloy (Fe-23Cr-0.39Mn-0.05Ti-0.09La, wt%), with Si and Al contents less than 0.01 wt%, and a second heat of Crofer (termed “New Crofer”) in which more care was used to reduce the Al and Si impurities, both provided by Dr. J. Quadakkers, Forschungszentrum, Jülich. E-brite and Fe-26Cr-Ferritic were also included in this experiment.

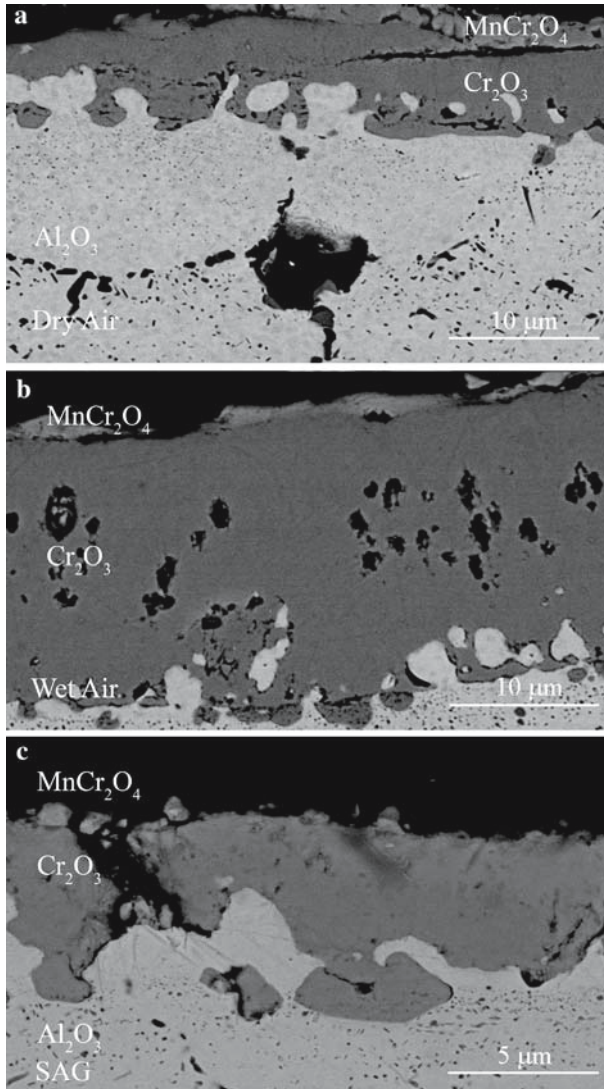


**Fig. 10.** Cross-section micrographs of Crofer after exposure in dry air (a), air + 10%  $\text{H}_2\text{O}$  (b), and  $\text{Ar}/\text{H}_2/\text{H}_2\text{O}$  (c) atmospheres at 900°C, showing more detail of the scales.

The cyclic oxidation kinetics in air with 10% water vapor are presented in Fig. 14. The Crofer from the original heat exhibited accelerated oxidation similar to that at 900°C whereas the Crofer from the second heat (with lower Si and Al impurities) and JS-3 did not exhibit this tendency. The 26 Cr

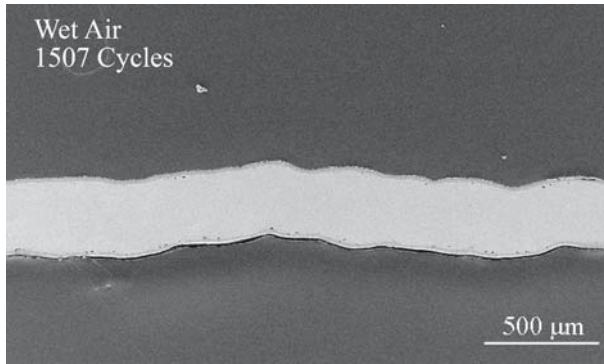


**Fig. 11.** Macroscopic photograph of a Crofer specimen exposed in air + 10% H<sub>2</sub>O showing extensive warpage.

Ferritic and E-brite began to show mass losses after short times as a combined result of spallation and scale evaporation.

Figure 15 is a cross-section micrograph of Crofer after exposure for 2000 h. It shows significant internal oxidation of Al and silica forming at the scale alloy interface. Figure 16 shows a cross-section of the purer Crofer from the second heat. There is substantially less internal oxidation but there is still a significant amount of metal protruding into the scale. Figure 17 shows a cross-section of JS-3. There is some internal oxidation but no metal protruding into the scale. Huczkowski et al.<sup>23</sup> observed most of the internal oxides to be TiO<sub>2</sub>. However, some of the particles in Fig. 17 are alumina and silica.

### Cyclic Oxidation at 700°C

Figures 18, 19, and 20 show the mass change vs. exposure time for samples at 700°C in dry air, Ar/H<sub>2</sub>/H<sub>2</sub>O, and air + 0.1 atm H<sub>2</sub>O, respectively. In all cases, AL 453 exhibited the largest mass gains, followed by Crofer and the 26 Cr Ferritic alloy. In the moist-air environment, the 26 Cr alloy showed small initial mass gains, but began to lose mass after ~400 cycles.

Figure 21 presents cross-section micrographs of Fe-26Cr Ferritic after exposures in all three atmospheres at 700°C. The scales are similar. The external scale consists of Cr<sub>2</sub>O<sub>3</sub> and there is a fine distribution of Al-rich precipitates in the alloy below the scale and Si-rich particles are present at the scale/alloy interface. The experimental mass change for Fe-26Cr Ferritic in wet air was observed to go negative after about 400 cycles. As was the case of the 900°C experiments, the mass changes in air + 0.1 atm H<sub>2</sub>O may



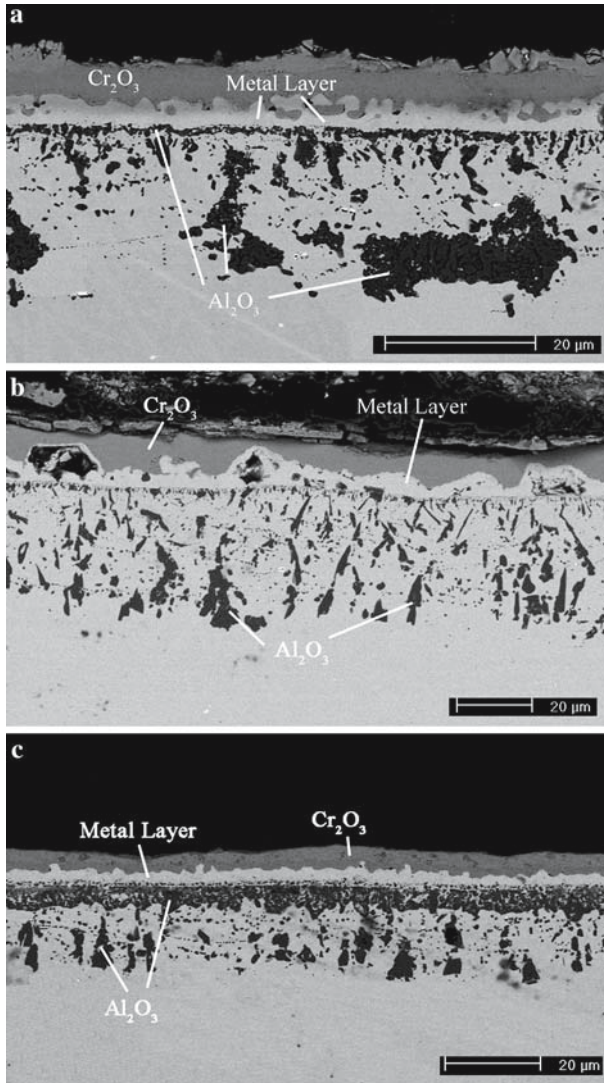


**Fig. 12.** Cross-section micrographs of AL453 after exposure in dry air (a), air + 10%  $\text{H}_2\text{O}$  (b), and Ar/ $\text{H}_2$ / $\text{H}_2\text{O}$  (c) atmospheres at 900°C.

be influenced by evaporation of  $\text{CrO}_2(\text{OH})_2$ , as will be discussed below. All of the Fe-26Cr specimens exposed at 700°C formed sigma-phase. The details of the formation of this undesirable brittle phase will be discussed in detail below.

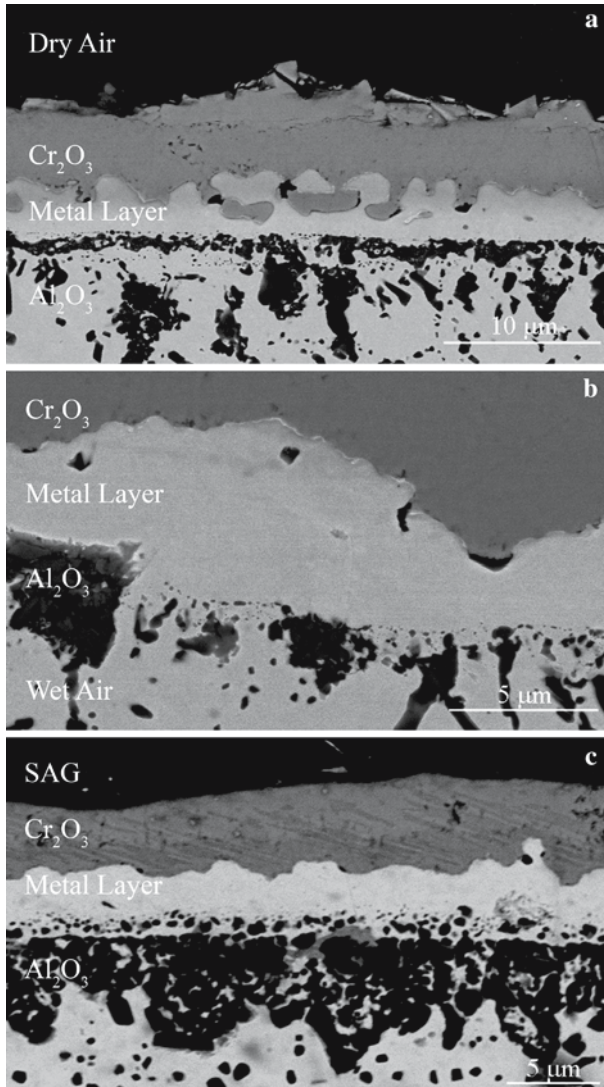


**Fig. 13.** Cross-section micrographs of AL453 after exposure in dry air (a), air + 10% H<sub>2</sub>O (b), and Ar/H<sub>2</sub>/H<sub>2</sub>O (c) atmospheres at 900°C, showing more detail of the scales.

Figure 22 presents cross-section micrographs of Crofer after exposure in all three environments. The specimen exposed in dry air had a layer of MnCr<sub>2</sub>O<sub>4</sub> at the scale/gas interface with a chromia layer beneath although the layer was not as well developed as that at 900°C. There was also

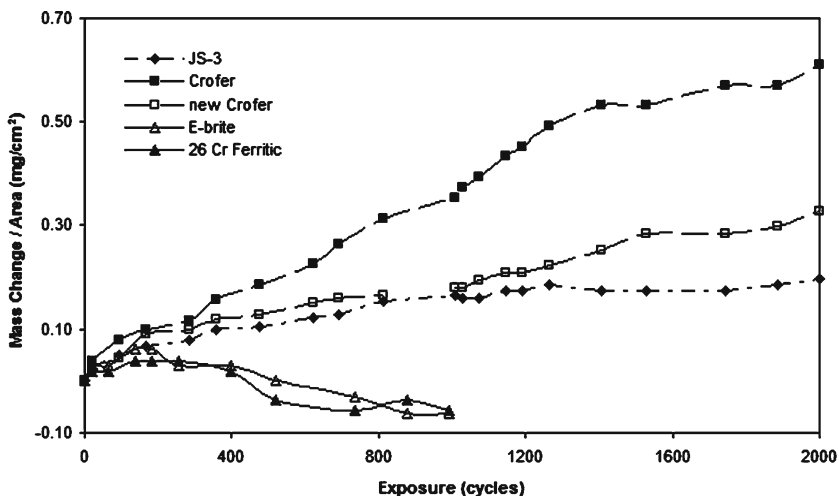


Fig. 14. Weight Change vs Time plots for duplicate specimens of ferritic alloys exposed in air + 10% H<sub>2</sub>O (simulated moistened cathode gas) at 800°C using 1-hour cycles.

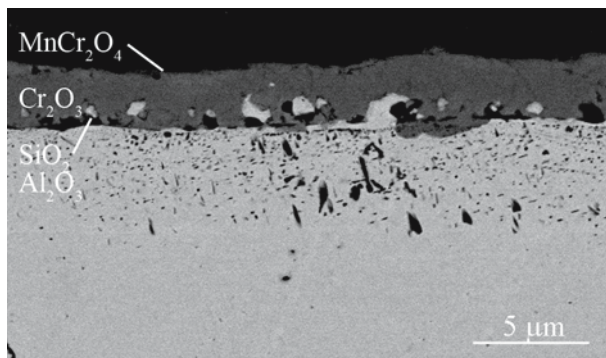


Fig. 15. Cross-section micrograph of Crofer after exposure in air + 0.1 atm H<sub>2</sub>O for 2000 h at 800°C.

formation of internal Al-rich oxides at this temperature, and these oxides had a tendency to form into semi-continuous bands. Bands of Si-rich oxides formed at the alloy/chromia interface.

Figure 23 presents cross-section micrographs of AL 453 exposed in the three environments. In all environments there was extensive internal oxidation of Al below the chromia scale, and these oxides formed virtually continuous films. Metallic regions were observed above the internal Al-oxides for the specimens exposed in air but were absent for exposures in SAG.

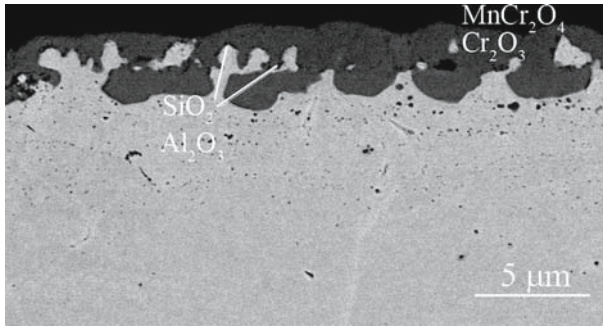


Fig. 16. Cross-section micrograph of "New Crofer" after exposure in air +0.1 atm H<sub>2</sub>O for 2000 h at 800°C.

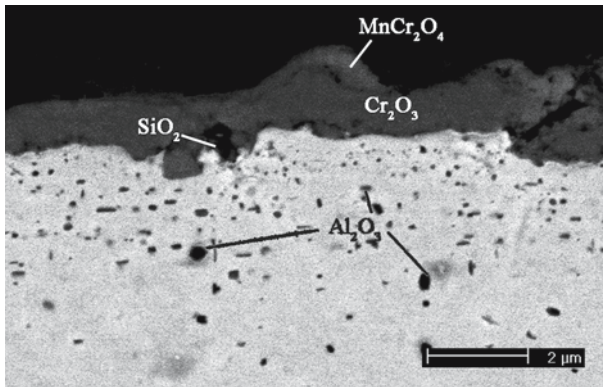
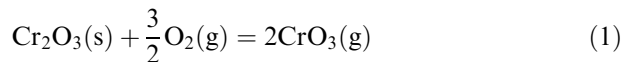


Fig. 17. Cross-section micrograph of JS-3 after exposure in air +0.1 atm H<sub>2</sub>O for 2000 h at 800°C.

### Oxide Evaporation

A significant problem with Cr (and chromia-forming alloys), which has been recognized for many years,<sup>7</sup> is the reactive evaporation of chromia scales. The formation of CrO<sub>3</sub> by the reaction



becomes significant at high temperatures and high oxygen pressures. The oxygen-pressure effect is illustrated in Fig. 1.<sup>8</sup> (In the presence of water vapor, the predominant evaporating species may become CrO<sub>2</sub> (OH)<sub>2</sub> whose partial pressure increases with increasing H<sub>2</sub>O partial pressure, as

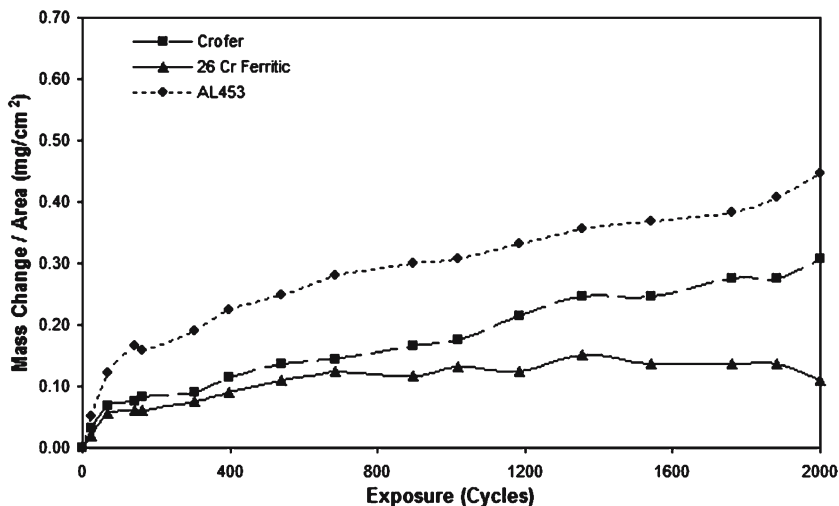


Fig. 18. Weight Change vs Time plots for duplicate specimens of ferritic alloys exposed in dry air (simulated cathode gas) at 700°C using 1-hour cycles.

indicated in Fig. 24.<sup>10</sup>) The evaporation of  $\text{CrO}_3$  results in the continuous removal of the protective  $\text{Cr}_2\text{O}_3$  scale so the diffusive transport through it is rapid. The effect of the volatilization on the oxidation kinetics has been

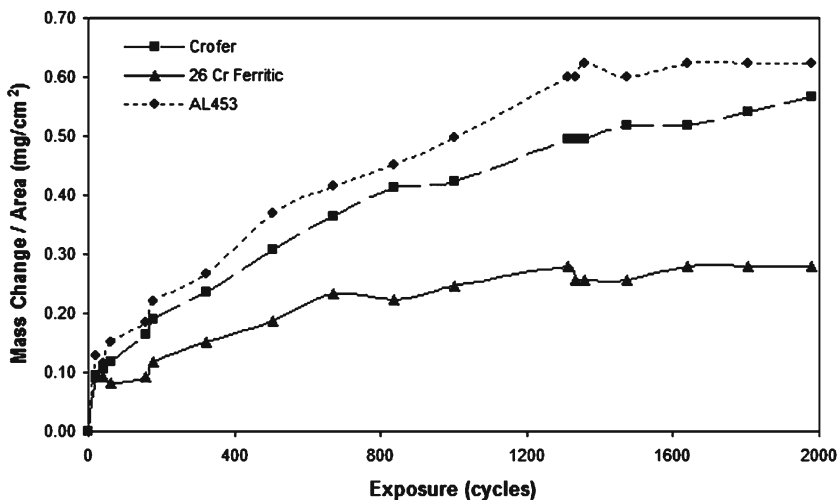


Fig. 19. Weight Change vs Time plots for duplicate specimens of three ferritic alloys exposed in  $\text{Ar}/\text{H}_2/\text{H}_2\text{O}$  (simulated anode gas) at 700°C using 1-hour cycles.

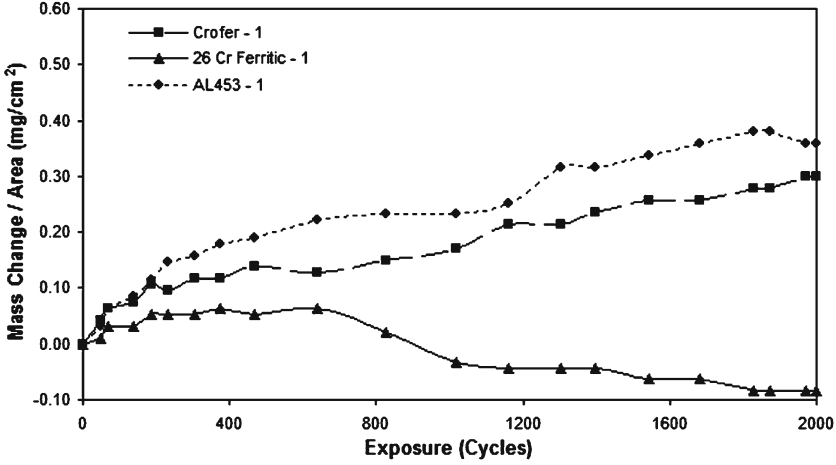


Fig. 20. Weight Change vs Time plots for duplicate specimens of ferritic alloys exposed in air + 10% H<sub>2</sub>O (simulated moistened cathode gas) at 700°C using 1-hour cycles.

analyzed by Tedmon.<sup>7</sup> The instantaneous change in scale thickness is the sum of two contributions: thickening due to diffusion and thinning due to volatilization.

$$\frac{dx}{dt} = \frac{k'_d}{x} - k'_s \quad (2)$$

where  $k'_d$  is a constant describing the diffusive process and  $k'_s$  describes the rate of volatilization. This equation can be rearranged to yield

$$\frac{dx}{\left(\frac{k'_d}{x} - k'_s\right)} = dt \quad (3)$$

which, upon integration, yields:

$$\frac{-x}{k'_s} - \frac{k'_d}{k'^2_s} \ln(k'_d - k'_s x) + C = t \quad (4)$$

where  $C$  is an integration constant to be evaluated from the initial conditions. Taking  $x = 0$  at  $t = 0$

$$t = \frac{k'_d}{k'^2_s} \left[ -\frac{k'_s}{k'_d} x - \ln\left(1 - \frac{k'_s}{k'_d} x\right) \right] \quad (5)$$

Initially, when the diffusion through a thin scale is rapid, the effect of CrO<sub>3</sub> volatilization is not significant, but as the scale thickens, the rate of

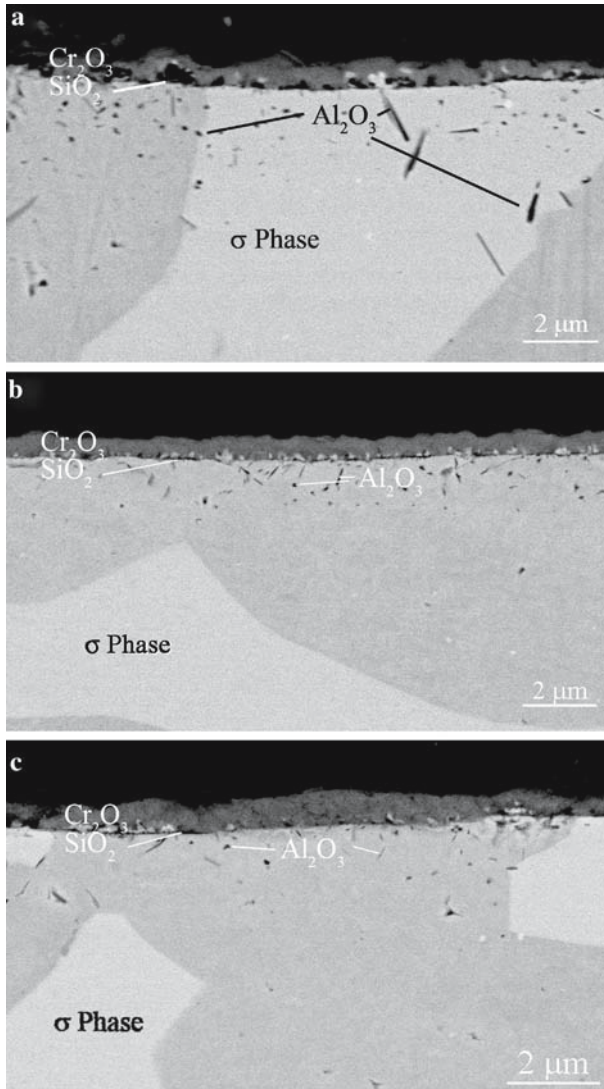


**Fig. 21.** Cross-section micrographs of Fe – 26% Cr ferritic alloy after exposure in atmospheres of dry air (a), Ar/H<sub>2</sub>/H<sub>2</sub>O (b), and air + 10% H<sub>2</sub>O (c) for 2000 one hour cycles at 700°C.

volatilization becomes comparable and then equal to the rate of diffusive growth. This situation, *paralinear oxidation*, results in a limiting scale thickness,  $x_o$ , for which  $dx/dt = 0$ . Setting this condition in equation 3 yields

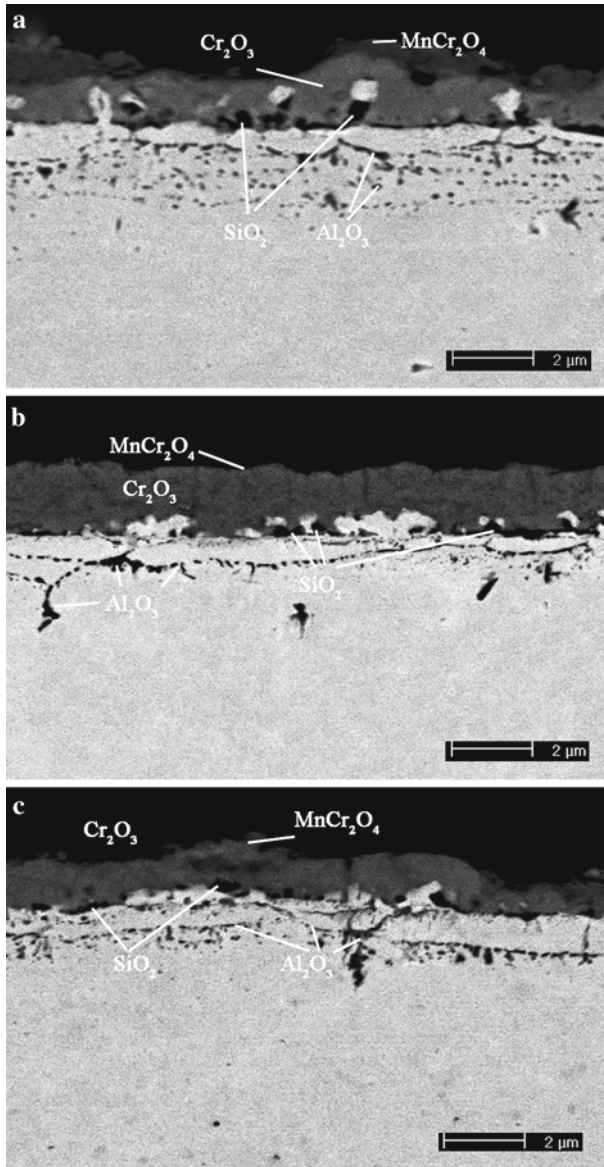


**Fig. 22.** Cross-section micrographs of Crofer 22APU after exposure in atmospheres of dry air (a), Ar/H<sub>2</sub>/H<sub>2</sub>O (b), and air + 10% H<sub>2</sub>O (c) for 2000 one hour cycles at 700°C.



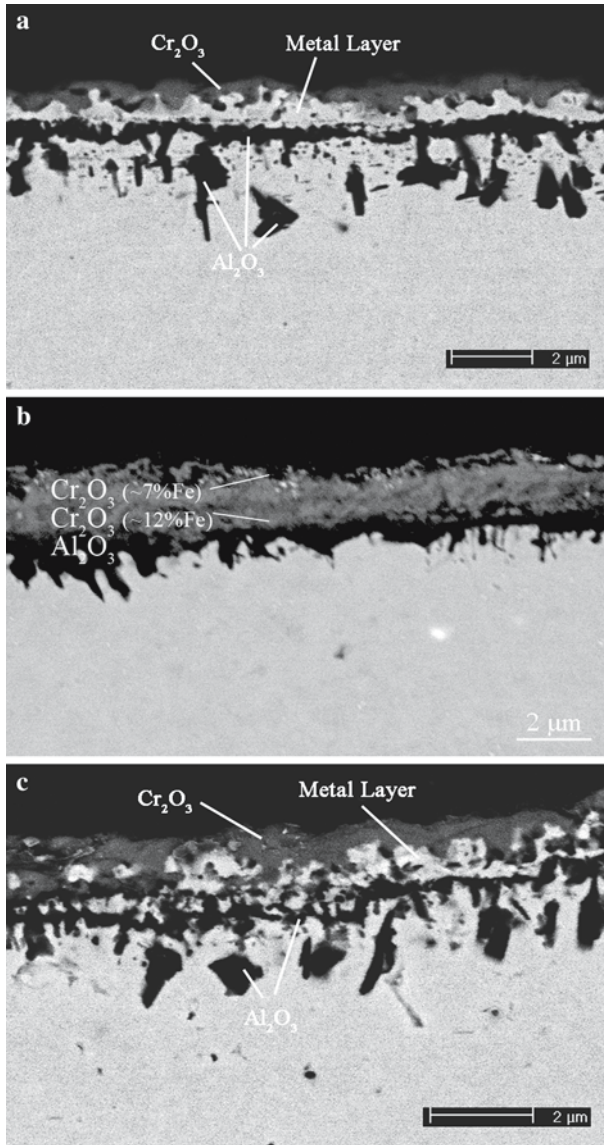


**Fig. 23.** Cross-section micrographs of AL 453 after exposure in atmospheres of dry air (a),  $\text{Ar}/\text{H}_2/\text{H}_2\text{O}$  (b.), and air + 10%  $\text{H}_2\text{O}$  (c.) for 2000 one hour cycles at 700°C.

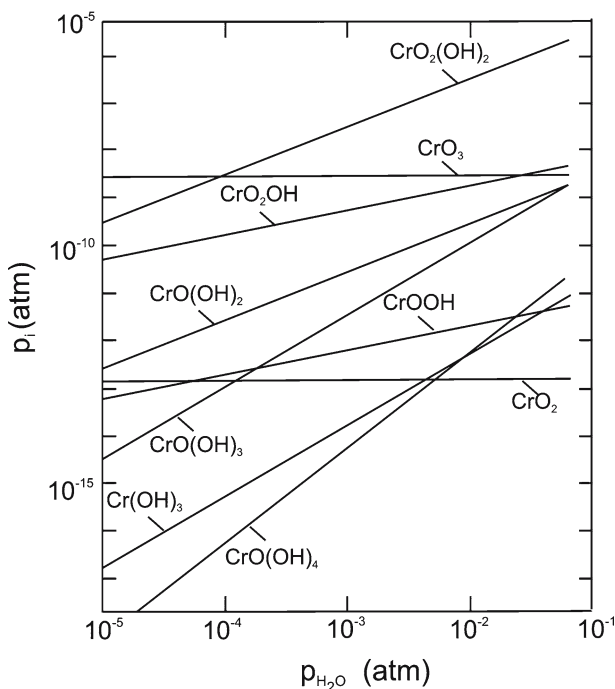


Fig. 24. Plot showing the effect of water vapor on the volatility of  $\text{Cr}_2\text{O}_3$  at  $950^\circ\text{C}$  after Ref. 10.

$$x_o = \frac{k'_d}{k'_s} \quad (6)$$

This problem, which is more serious in rapidly flowing gases, is one of the major limitations on the high temperature use of  $\text{Cr}_2\text{O}_3$  forming alloys and coatings.

Evaporation is a particular problem in the cathode gas of solid oxide fuel cells (SOFCs) since the  $\text{CrO}_3$  partial pressure increases with oxygen partial pressure, as illustrated in Fig. 1. The volatile species are reduced at electrochemically active sites on the cathode during SOFC operation, which inhibits the required oxygen reduction.<sup>8</sup> Analysis of the Cr-vapor species<sup>10</sup> indicates water contents above about 0.1% in air result in partial pressures of  $\text{CrO}_2(\text{OH})_2$  which exceed the partial pressure of  $\text{CrO}_3$ . Thus, maintaining the cathode gas as dry as possible is desirable.

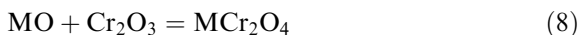
Figures 1 and 24 are constructed for unit activities of Cr and  $\text{Cr}_2\text{O}_3$ , i.e. evaporation at high oxygen partial pressures occurs from pure chromia. However, examination of the equilibrium constant for reaction 1

$$K_1 = \frac{p_{\text{Cr}_2\text{O}_3}^2}{a_{\text{Cr}_2\text{O}_3} p_{\text{O}_2}^{3/2}} \quad (7)$$

shows that, for a fixed oxygen partial pressure, the partial pressure of  $\text{Cr}_2\text{O}_3$  will decrease as the activity of chromia is reduced. Other things being equal, the evaporation rate should be directly proportional to the  $\text{Cr}_2\text{O}_3$  partial pressure. Therefore, the presence of an outer oxide layer with reduced chromia activity could slow the scale evaporation. Coatings of  $\text{La}_{0.9}\text{Sr}_{0.1}\text{CrO}_3$  have been applied to ferritic alloys to limit  $\text{Cr}_2\text{O}_3$  evaporation.<sup>24</sup>

The formation of a complex oxide over a chromia layer can also occur naturally during oxidation of some alloys. Spinel ( $\text{MCr}_2\text{O}_4$ ) have been observed to form over chromia scales growing on alloys containing the transition metals Fe, Ni, Co, and Mn. In some cases the spinels form before the chromia layer becomes continuous (transient oxidation), but in others the spinel forms by outward diffusion of the transition metal through the chromia layer. Outer layers containing Fe and Mn have been known to form on stainless steels for many years.<sup>25</sup> This is somewhat remarkable since the steel usually only contain about 1% Mn. The high mobility of Mn ions in chromia is also in agreement with theoretical studies.<sup>26</sup> Crystal-field theory calculations of the difference in stabilization energies for cations on octahedral versus tetrahedral sites in the hexagonal oxide ion sublattice of chromia lead to the prediction that the mobility of divalent cations should increase in the order  $\text{Ni}^{2+}:\text{Cu}^{2+}:\text{Co}^{2+}:\text{Fe}^{2+}:\text{Mn}^{2+}$ .<sup>26</sup> Figure 9 shows cross-sectional micrographs of Crofer 22, which contains approximately 0.5 wt% Mn, after exposure at 900°C in dry air. An outer layer of  $\text{MnCr}_2\text{O}_4$  can be observed at the scale/gas interface. This layer is particularly well developed for the specimen oxidized in dry air.

The diffusion properties in the chromia will control the development of an outer spinel layer, but the thermodynamic properties of the individual spinels will determine how much they decrease the activity of chromia. Tretjakow and Schmalzried<sup>27</sup> performed an extensive study of the thermodynamic properties of the spinels of Cr with Fe, Ni, Co, Mg, and Cu over the temperature range 1000–1500 K. They found that the standard Gibbs free energy change for the reaction

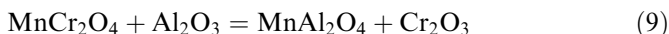


was very similar for all the spinels, which would suggest they all would be similarly effective in lowering the activity of chromia. Unfortunately, Mn was not included in this study, and no data are listed for  $\text{MnCr}_2\text{O}_4$  in the available thermodynamic data compilations.<sup>28</sup> In the present study the

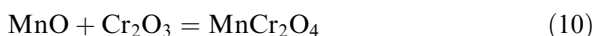
available thermodynamic data<sup>28</sup> were used to catalog the properties of the spinels for which data are available and then to estimate the thermodynamic data for  $\text{MnCr}_2\text{O}_4$ . The data were used to estimate the partial pressure of  $\text{CrO}_3$  which would stand in equilibrium with each spinel at typical SOFC operating temperatures.

### Thermodynamic Calculations

The standard Gibbs free energies of formation ( $\Delta G^\circ$ ) for  $\text{Cr}_2\text{O}_3$ ,  $\text{Al}_2\text{O}_3$ ,  $\text{FeO}$ ,  $\text{NiO}$ ,  $\text{CoO}$ ,  $\text{MnO}$ ,  $\text{MgO}$ ,  $\text{FeCr}_2\text{O}_4$ ,  $\text{NiCr}_2\text{O}_4$ ,  $\text{CoCr}_2\text{O}_4$ ,  $\text{MgCr}_2\text{O}_4$ , and  $\text{MnAl}_2\text{O}_4$ , were taken from reference 28 over the temperature range of interest 1000–1300 K. Data for the reaction



were reported at one temperature (1373 K) in reference.<sup>29</sup> This allowed the calculation of  $\Delta G^\circ$  for  $\text{MnCr}_2\text{O}_4$  at 1373 K and estimates of the standard entropy change ( $\Delta S^\circ$ ) for the reaction



were used to extrapolate the data to lower temperatures. Figure 25 shows  $\Delta G^\circ$  for reaction 8 for Fe, Ni, Co, and Mg. The data for Fe, Ni, and Mg are similar while the values for Co are somewhat more negative. Fig. 26 presents the extrapolated data for Mn with the data for Ni as a basis for comparison. It is clear that  $\text{MnCr}_2\text{O}_4$  is much more stable than the other spinels. The data from Fig. 26 were used to calculate the equilibrium constant for reaction 10 which allowed the calculation of the activity of chromia, assuming saturation with MnO. Insertion of this value in equation 7 allowed calculation of the  $\text{CrO}_3$  partial pressure in equilibrium with  $\text{MnCr}_2\text{O}_4$  in air. These values are plotted in Fig. 27 along with those for unit activity of chromia and those for  $\text{LaCrO}_3$ . (The latter were calculated by inserting the activity data for chromia in  $\text{LaCrO}_3$  from reference<sup>10</sup> and presumably refer to  $\text{La}_2\text{O}_3$ -saturation.) Figure 27 indicates that the  $\text{CrO}_3$  partial pressure, and therefore, the evaporation rate from a chromia forming alloy could be reduced by two orders of magnitude if a layer of MnO-saturated  $\text{MnCr}_2\text{O}_4$  could be made to reliably form on the surface. A dense, artificially applied coating of  $\text{LaCrO}_3$  could, in principle, achieve another order of magnitude reduction.

It should be noted that the low values of  $\text{CrO}_3$  partial pressure indicated to be in equilibrium with  $\text{MnCr}_2\text{O}_4$  and  $\text{LaCrO}_3$  in Fig. 27 were calculated assuming MnO and  $\text{La}_2\text{O}_3$  saturation, respectively. If layers of these compounds are present over a chromia film and begin to equilibrate

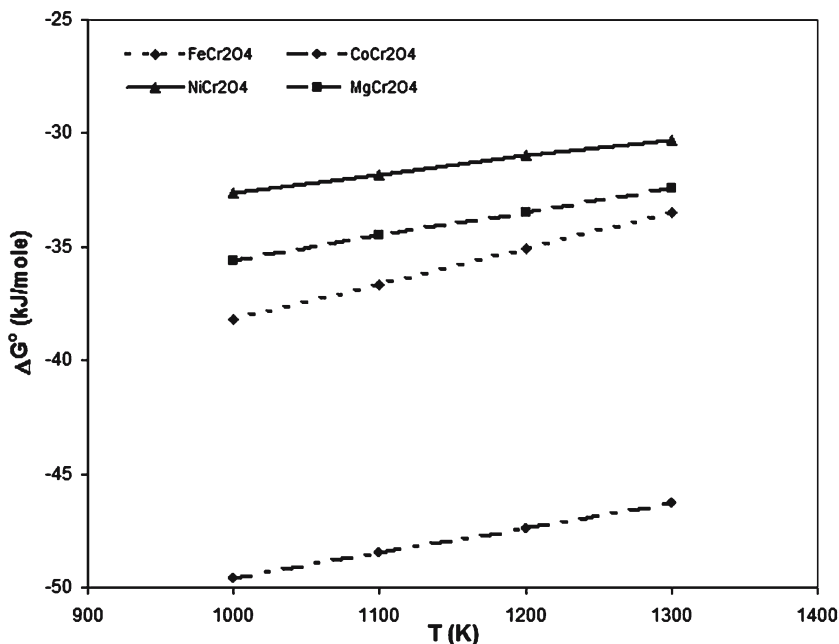


Fig. 25. Standard free energy as a function of temperature changes for the reaction of transition metal oxides with chromia to form spinel.

with the underlying chromia the activity of chromia will increase and this will result in an increase in the  $\text{CrO}_3$  partial pressure. In the limit of the layers becoming  $\text{Cr}_2\text{O}_3$  saturated the chromia activity will be unity, and the  $\text{CrO}_3$  partial pressure will be given by the line for  $\text{Cr}_2\text{O}_3$  in Fig. 27. The rate and extent of such equilibration will be determined by transport in the outer layer as well as loss of  $\text{CrO}_3$  to the gas phase.

All of the above comments will also pertain to the reduction of the partial pressure of  $\text{CrO}_2(\text{OH})_2$  over chromia-containing spinels in atmospheres containing water vapor.

### Formation of Oxide-free Zone Below the Chromia Scale

A number of the cross-section micrographs presented above indicate oxide-free metallic regions between the external chromia scale and a zone of internal oxidation. In the case of Crofer these regions were in the form of metallic globules protruding into the chromia scale, Figs. 9, 10, 15, 16 and 22. In the case of AL 453 a continuous, or nearly continuous, region formed below the chromia scale, Figs. 12, 13, and 23.

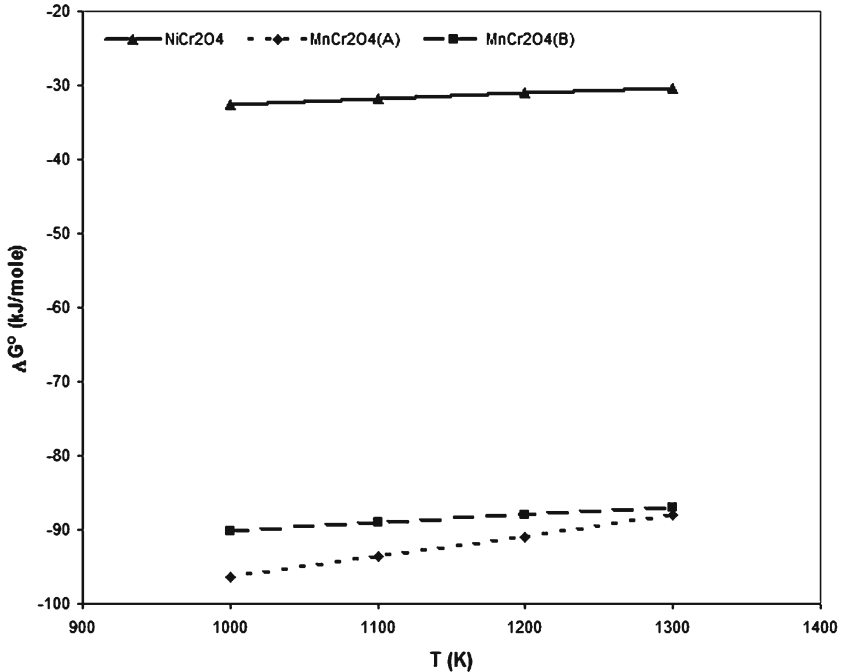


Fig. 26. Standard free energy changes for the reactions of NiO and MnO with chromia to form the respective chromates. (The two lines for  $\text{MnCr}_2\text{O}_4$  were obtained by using two different techniques for estimating  $\Delta S^\circ$ .)

These regions have formed by plastic flow of metal from the zone of internal oxidation because of stresses produced by the volume increase associated with the internal oxide particles. This phenomenon was apparently first reported by Darken<sup>30</sup> for the internal oxidation of Ag-base alloys. It was studied in detail by Guruswamy et al.<sup>31</sup> who observed oxide-free Ag nodules on the surface of Ag-In alloys after internal oxidation in air at temperatures in the range 500–700°C. It was proposed that dislocation pipe-diffusion controlled creep was the mode of stress relief and Ag transport. Similar observations have been made for the internal oxidation of Ni–Al<sup>32</sup> and Ni–Al–Si<sup>33,34</sup> alloys. The amount of metal transported has been observed to be proportional to the volume of internal oxides produced. This is qualitatively the result of the current investigation in that there is a much larger oxide-free region for AL453 than Crofer which is consistent with a larger internal oxide volume for AL453. Such a region has apparently formed locally above a single large internal oxide particle in 26 Cr Ferritic in Fig. 21a. The previous observations of this phenomenon have generally

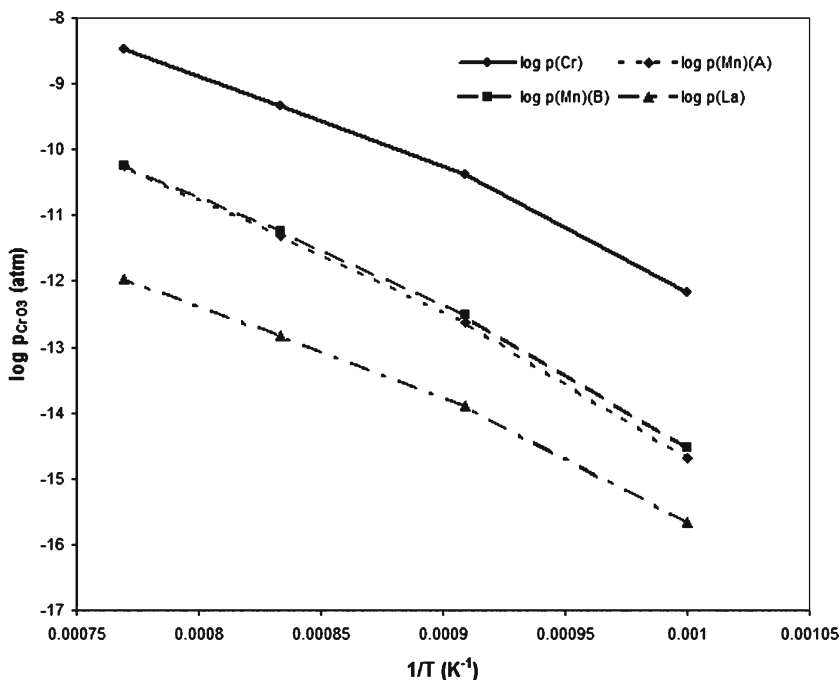
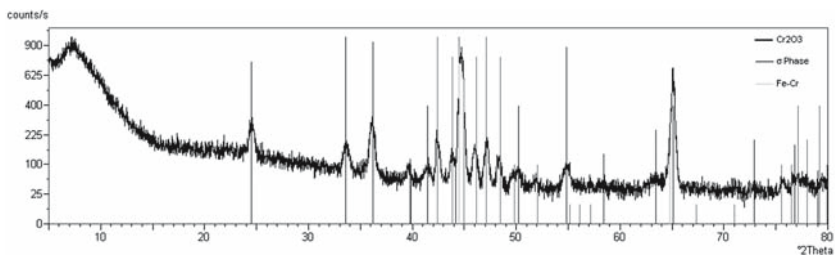


Fig. 27. Partial pressures of  $\text{CrO}_3$  in equilibrium with  $\text{Cr}_2\text{O}_3$ ,  $\text{La}_2\text{O}_3$ -saturated  $\text{LaCrO}_3$ , and  $\text{MnO}$ -saturated  $\text{MnCr}_2\text{O}_4$  as a function of temperature.

been for the case of internal oxidation with no external scale formation. Guan et al.<sup>35</sup> studied the internal oxidation of Ni–Al–Si alloys under a NiO scale but did not report an oxide-free region for an oxidation temperature which had produced an oxide-free layer of Ni on the surface in the absence of an external scale. Huczowski et al.<sup>23</sup> show several examples of metallic protrusions under chromia scales and comment that they can accelerate the oxidation rate.

### Sigma-Phase Formation

Figure 21 shows that a second phase formed in the Fe-26 Cr ferritic alloy during exposure at 700°C. Figure 28 shows the XRD pattern for a Fe-26 Cr ferritic specimen exposed for 2000 hours at 700°C in air + 0.1 atm  $\text{H}_2\text{O}$ . Many of the peaks match with the chromia lines, the ferrite lines, or the sigma phase lines. This analysis proved that the sample did in fact contain the sigma phase.



**Fig. 28.** X-ray diffraction pattern for 26 Cr Ferritic alloy exposed at 700°C in air + 0.1 atm H<sub>2</sub>O for 2000 h.

The approximate compositions of the sigma phase and the ferrite were determined by EDS analysis. The results show significant increases in the amount of chromium (~35 wt%) and molybdenum (3–4 wt%) in the sigma phase regions when compared to the initial composition. The surrounding ferrite is slightly depleted of those elements. The silicon content appears to not be greatly affected, with only a slight enrichment in the sigma phase.

Figure 29 shows E-brite that had been exposed in dry air at 700°C in 50 h increments to 500 h. Only a small amount of the sigma phase is seen after 200 h, but with time, more is seen in each successive micrograph. The sigma phase nucleates at intersections of ferrite grain boundaries with the free surface and propagates inward.

The micrographs of Fe-26 Cr ferritic exposed in dry air at 700°C in 50 h increments up to 500 h are shown in Fig. 30. Again, there is only a small amount of sigma phase observed in the sample exposed for 200 h. As the exposure time is increases, the amount of sigma phase also increases.

The sigma phase was observed only in E-brite and Fe-26Cr ferritic that had been exposed at 700°C in the three atmospheres that were studied. This can be explained if the Fe–Cr phase diagram is examined (see Fig. 31). E-brite and Fe-26Cr ferritic both contain 26% chromium, which is more than the other alloys that were investigated. In Fig. 31, point A (700°C, 26% chromium) is within the region where sigma forms, but point B (900°C, 26% chromium) is outside of this region. However, sigma phase formation is also strongly influenced by other elements in the alloy.

E-brite contains 1.0% molybdenum and 0.2% silicon. The Fe-26 Cr ferritic also contains 1.0% molybdenum, but has approximately 1.0% silicon. Additions of molybdenum and silicon will increase the rate of sigma-phase formation.<sup>36</sup> However, Fe-26 Cr ferritic contains considerably more silicon than E-brite. It has been reported that Si is extremely potent in accelerating sigma-phase formation.<sup>37,38</sup> This was indeed observed in that



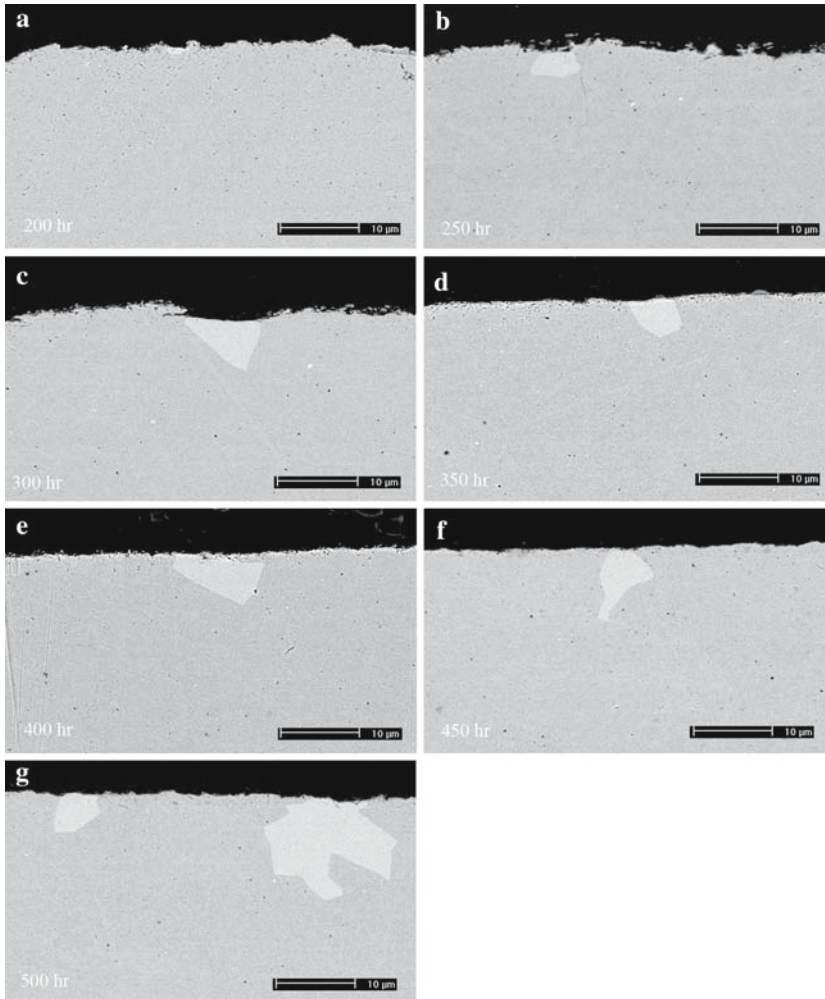


**Fig. 29.** Cross-sections of E-brite exposed at 700°C in dry air in 50 h increments after (a) 200 h, (b) 250 h, (c) 300 h, (d) 350 h, (e) 400 h, (f) 450 h, and (g) 500 h.

the formation of sigma phase was more extensive in Fe-26Cr ferritic than E-brite. Tetsui et al.<sup>38</sup> have reported that a high-purity Fe-30Cr alloy did not form sigma phase after 500 h at 650°C. Therefore, alloy purity may be an important avenue of study for production of high-Cr interconnects which are resistant to sigma-phase formation.

The development of the sigma phase was observed to be strongly influenced by the environment in which the specimens were exposed.

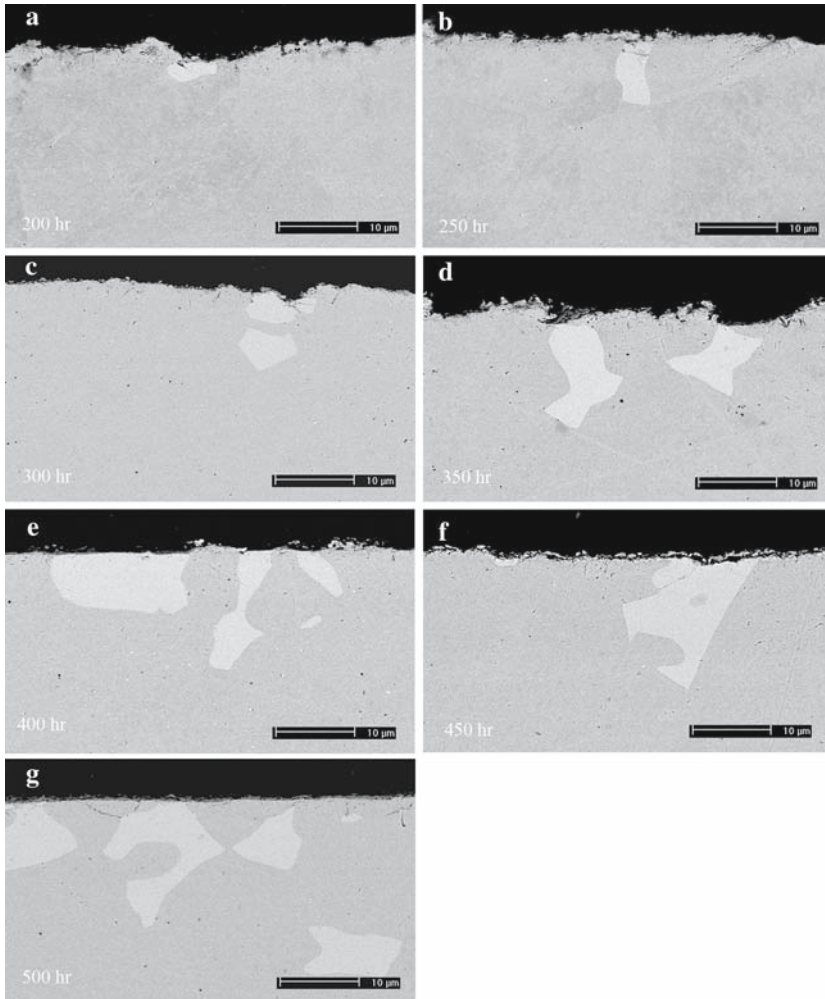


**Fig. 30** Cross-sections of 26 Cr Ferritic exposed at 700°C in dry air in 50 h increments after (a) 200 h, (b) 250 h, (c) 300 h, (d) 350 h, (e) 400 h, (f) 450 h, and (g) 500 h.

Figure 32 shows a cross-section of Fe-26Cr ferritic which was exposed in dry air for 2000 cycles. The sigma phase, which nucleated at the surface, has penetrated a distance of approximately 50 µm into the alloy. Figure 33 show a cross-section of the same alloy which was exposed in simulated anode gas for 2000 cycles. Sigma phase was observed to form all the way to the center of the 1 mm-thick specimen. Similarly, Fig. 34 shows the cross-section of a specimen exposed for 2000 cycles in air plus 10% water vapor.

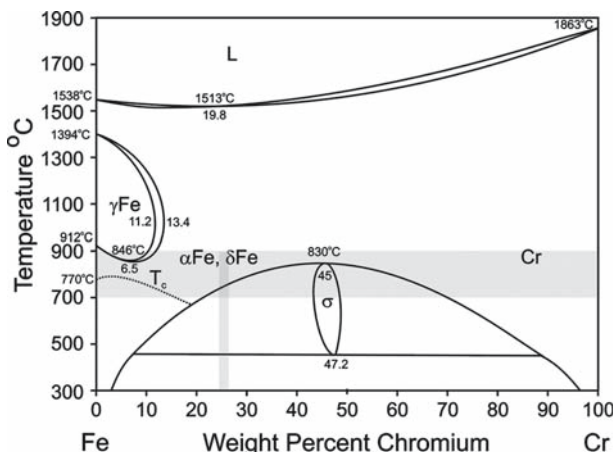


Fig. 31. The Fe-Cr phase diagram showing regions in which  $\sigma$ -phase can form.

The sigma phase has formed all the way to the center of the specimen and the volume fraction of sigma phase appears to be even larger than that in Fig. 33. Figures 33 and 34 suggest that the presence of water vapor is influencing the nucleation and/or growth of the sigma phase. This somewhat remarkable result of a metallic phase transformation being influenced by an external atmosphere is the subject of continuing experiments.

### SUMMARY AND CONCLUSIONS

The cyclic oxidation of a variety of ferritic stainless steels has been studied in the temperature range 700–900°C in atmospheres relevant to

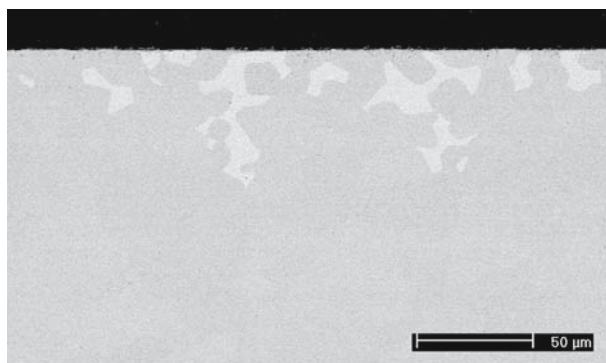
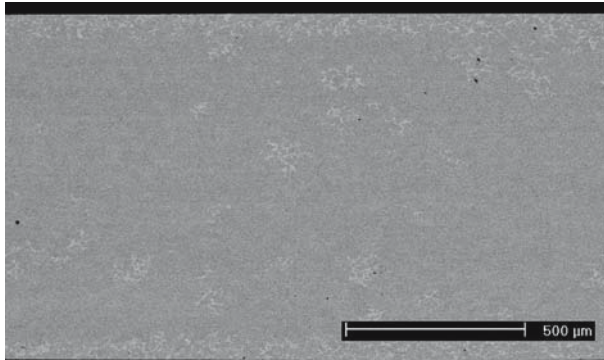
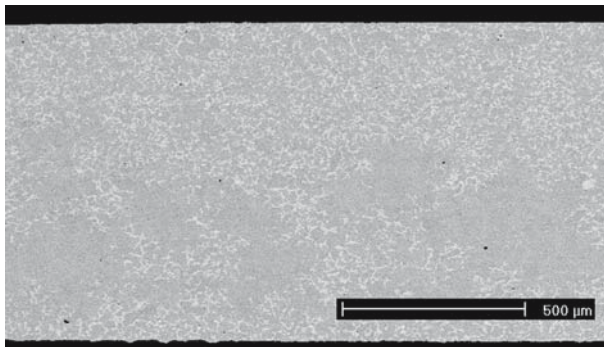


Fig. 32. Cross-section of 26 Cr Ferritic exposed at 700°C in dry air for 2000 h showing  $\sigma$ -phase only formed near the surface.



**Fig. 33.** Cross-section of 26 Cr Ferritic exposed at 700°C in Ar/H<sub>2</sub>/H<sub>2</sub>O for 2000 h showing  $\sigma$ -phase formed throughout the cross-section.



**Fig. 34.** Cross-section of 26 Cr Ferritic exposed at 700°C in air +0.1 atm H<sub>2</sub>O for 2000 h showing  $\sigma$ -phase formed throughout the cross-section.

solid-oxide fuel-cell operation. The most detrimental environment at 800°C and 900°C was found to be air with 10% water vapor. This resulted in excessive oxide spallation from Fe-26Cr ferritic and E-brite and rapid scale growth on Crofer22 APU and AL 453. The oxidation behavior of the alloys varied considerably based on the Cr concentration and the presence of other minor elements, whether added intentionally (e.g. reactive elements) or remaining as impurities (e.g. Si, Al).

Oxide growth was slow at 700°C but the higher-Cr-content alloys were observed to form sigma phase at this temperature. The sigma phase

formation was accelerated by higher silicon contents and, remarkably, by the presence of water vapor in the exposure environment.

Alloys containing Mn were observed to form an outer layer of  $\text{MnCr}_2\text{O}_4$  over the chromia scale. The potential for this overlayer to suppress reactive evaporation of the chromia scales has been analyzed.

### ACKNOWLEDGMENTS

Financial support of this research by the U. S. Department of Energy through SECA Award No. DE-FC26-02NT41578 and contributions of alloys by P. Singh and Z. Yang (Pacific Northwest National Laboratory), J. Rakowski (ATI Allegheny Ludlum), and J. Quadakkers (Research Center – Jülich) are gratefully acknowledged.

### REFERENCES

1. Z. G. Yang, J. W. Stevenson, and P. Singh *Advanced Materials and Processes*, **161**(6), p. 34 (2003).
2. W. Z. Zhu, and S. C. Deevi *Materials Science and Engineering*, **A348**, p. 227 (2003).
3. Z. G. Yang, K. S. Weil, D. M. Paxton, and J. W. Stevenson *Journal of the Electrochemical Society*, **150**, p. A1188 (2003).
4. W. J. Quadakkers, J. Piron-Abellan, V. Shemet, and L. Singheiser *Materials at High Temperatures*, **20**, p. 115 (2003).
5. D. M. England, and A. V. Virkar *Journal of the Electrochemical Society*, **146**, p. 3196 (1999).
6. W. J. Quadakkers, H. Greiner, and W. Köck, *Metals and Alloys for High Temperature SOFC Application* in Proc. First European Solid Oxide Fuel Cell Forum, U. Bossel, ed. 1994, p. 525.
7. C. S. Tedmon *Journal of the Electrochemical Society*, **113**, p. 766 (1966).
8. N. Birks, and G. H. Meier, *Introduction to High Temperature Oxidation of Metals* (London: Edward Arnold, 1983).
9. W. J. Quadakkers, H. Greiner, W. Köck, H. P. Buchkremer, K. Hilpert, and D. Stöver, *The Chromium Base Metallic Bipolar plate – Fabrication, Corrosion and Cr Evaporation*. in Proc. Second European Solid Oxide Fuel Cell Forum, B. Thorstensen, ed. 1996, p. 297.
10. K. Hilpert, D. Das, M. Miller, D. H. Peck, and R. Weiss *Journal of the Electrochemical Society*, **143**, p. 3642 (1996).
11. K. Huang, P. Y. Hou, and J. B. Goodenough *Solid State Ionics*, **129**, p. 237 (2000).
12. T. Brylewski, M. Nanko, T. Maruyama, and K. Przybylski *Solid State Ionics*, **143**, p. 131 (2001).
13. W. J. Quadakkers, T. Malkow, J. Pirón-Abellán, U. Flesch, V. Shemet, and L. Singheiser, *Suitability of Ferritic Steels for Application as Construction Materials for SOFC Interconnects*. in Proc. Fourth European Solid Oxide Fuel Cell Forum, A.J. McEvoy, ed. 2000, p. 827.
14. J. Pirón-Abellán, V. Shemet, F. Tietz, L. Singheiser, W. J. Quadakkers, and A. Gil, *Ferritic Steel Interconnect for Reduced Temperature SOFC*. in Proc. Solid Oxide Fuel Cells VII, H. Yokokawa and S.C. Singhal, eds. (The Electrochem. Soc., 2001, p. 811).

15. Z. G. Yang, J. S. Hardy, M. S. Walker, G. Xia, S. P. Simner, and J. W. Stevenson *Journal of the Electrochemical Society*, **151**, p. A1825 (2004).
16. D. M. England, and A. V. Virkar *Journal of the Electrochemical Society*, **148**, p. A330 (2001).
17. A. Gil, H. J. Penkalla, M. Hänsel, J. Norton, W. Köck, and W. J. Quadackers, *The Oxidation Behaviour of Cr Based ODS Alloys in H<sub>2</sub>/H<sub>2</sub>O at 1000°C*. in IX Conf. On Electron Microscopy of Solids, 1996, p. 441.
18. W. J. Quadackers, J. F. Norton, J. Penkalla, U. Breuer, A. Gil, T. Rieck, and M. Hänsel, *SNMS and TEM Studies on the Oxidation Behaviour of Cr-Based ODS Alloys*. in Microscopy of Oxidation 3, S.B. Newcomb and J. A. Little, eds., Inst. of Materials, 1996, p. 221.
19. W. J. Quadackers, J. F. Norton, S. Canetoli, K. Schuster, and A. Gil, *Hot Stage Microscopy of the Nucleation and Growth of Oxide Scales on Cr and Cr-Based Alloys*. in Microscopy of Oxidation 3, S. B. Newcomb and J. A. Little, eds., Inst. of Materials, 1996, p. 609.
20. R. Janakiraman, G. H. Meier, and F. S. Pettit *Metallurgical and Materials Transactions A*, **30A**, p. 2905 (1999).
21. M. C. Maris-Sida, G. H. Meier, and F. S. Pettit *Metallurgical and Materials Transactions A*, **34A**, p. 2609 (2003).
22. Z. G. Yang, M. S. Walker, P. Singh, and J. W. Stevenson *Electrochemistry and Solid State Letters*, **6**, p. B35 (2003).
23. P. Huczkowski, N. Christiansen, V. Shemet, J. Piron-Abellan, L. Singheiser, and W. J. Quadackers *Journal of Fuel Cell Science and Technology (Trans. ASME)*, **1**, p. 31 (2004).
24. C. Gindorf, L. Singheiser, and K. Hilpert *Steel Research*, **72**, p. 528 (2001).
25. J. E. Antill, K. A. Peakall, and J. B. Warburton *Corrosion Science*, **8**, p. 689 (1968).
26. M. G. C. Cox, B. McEnaney, and V. D. Scott *Philosophical Magazine*, **26**, p. 839 (1972).
27. J. D. Tretjakow, and H. Schmalzried *Berichte der Bunsengesellschaft*, **69**, p. 396 (1965).
28. I. Barin, *Thermochemical Data of Pure Substances* (VCH Verlagsgesellschaft: Weinheim, 1993).
29. T. Jacob, and G. N. K. Iyengar *Journal of the American Ceramic Society*, **69**, p. 487 (1986).
30. L. S. Darken *Transaction of the American Society Metals*, **54**, p. 600 (1961).
31. S. Guruswamy, S. M. Park, J. P. Hirth, and R. A. Rapp *Oxidation of Metals*, **26**, p. 77 (1986).
32. F. H. Stott, and G. C. Wood *Materials Science and Technology*, **4**, p. 1072 (1988).
33. H. C. Yi, S. W. Guan, W. W. Smeltzer, and A. Petric *Acta Metallurgica et Materialia*, **42**, p. 981 (1994).
34. S. W. Guan, H. C. Yi, and W. W. Smeltzer *Oxidation of Metals*, **41**, p. 377 (1994).
35. S. W. Guan, H. C. Yi, and W. W. Smeltzer *Oxidation of Metals*, **41**, p. 389 (1994).
36. G. F. Van der Voort, *Embrittlement of Steels* in ASM Handbook, Volume 1, Properties and Selection: Irons, Steels, and High-Performance Alloys, 10th edn. (ASM International, Materials Park, Ohio, 1990) pp. 689–736.
37. I. Yano, and K. Abiko *Physica Status Solidi*, **160**, p. 449 (1997).
38. T. Tetsui, M. Shinohara, and K. Abiko *Physica Status Solidi*, **160**, p. 459 (1997).